Inorganic Chemistry

pubs.acs.org/IC Article

Non-Native Anionic Ligand Binding and Reactivity in Engineered Variants of the Fe(II)- and α -Ketoglutarate-Dependent Oxygenase, SadA

Natalie H. Chan, Christian A. Gomez, Vyshnavi Vennelakanti, Qian Du, Heather J. Kulik, and Jared C. Lewis*



Cite This: Inorg. Chem. 2022, 61, 14477–14485



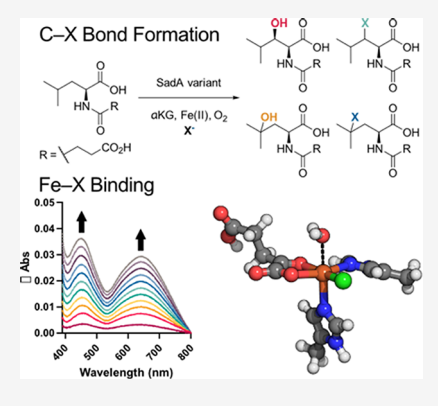
ACCESS I

III Metrics & More

Article Recommendations

Supporting Information

ABSTRACT: Mononuclear non-heme Fe(II)- and α -ketoglutarate-dependent oxygenases (FeDOs) catalyze a site-selective C—H hydroxylation. Variants of these enzymes in which a conserved Asp/Glu residue in the Fe(II)-binding facial triad is replaced by Ala/Gly can, in some cases, bind various anionic ligands and catalyze non-native chlorination and bromination reactions. In this study, we explore the binding of different anions to an FeDO facial triad variant, SadX, and the effects of that binding on HO $^{\bullet}$ vs X $^{\bullet}$ rebound. We establish not only that chloride and bromide enable non-native halogenation reactions but also that all anions investigated, including azide, cyanate, formate, and fluoride, significantly accelerate and influence the site selectivity of SadX hydroxylation catalysis. Azide and cyanate also lead to the formation of products resulting from N $_3^{\bullet}$, NCO $^{\bullet}$, and OCN $^{\bullet}$ rebound. While fluoride rebound is not observed, the rate acceleration provided by this ligand leads us to calculate barriers for HO $^{\bullet}$ and F $^{\bullet}$ rebound from a putative Fe(III)(OH)(F) intermediate. These calculations suggest that the lack of fluorination is due to the relative barriers of the HO $^{\bullet}$ and F $^{\bullet}$ rebound transition states rather than an



inaccessible barrier for F[•] rebound. Together, these results improve our understanding of the FeDO facial triad variant tolerance of different anionic ligands, their ability to promote rebound involving these ligands, and inherent rebound preferences relative to HO[•] that will aid efforts to develop non-native catalysis using these enzymes.

INTRODUCTION

Mononuclear non-heme Fe(II)- and α -ketoglutarate (α KG)-dependent oxygenases (FeDOs) catalyze site-selective C–H hydroxylation via C–H abstraction by a high-valent Fe(IV)-oxo intermediate, followed by the rebound of HO $^{\bullet}$ from the resulting Fe(III)-hydroxo species (Figure 1, outer cycle). The Fe(IV)-oxo intermediate is generated by the Fe(II)-mediated reaction of O₂ with α -ketoglutarate, which generates CO₂ and succinate as byproducts. These enzymes adopt a cupin fold containing a conserved His-X-Asp/Glu-X_n-His motif that forms a facial triad coordination site to bind Fe(II). This same motif is used by other Fe(II)- and α KG-dependent oxygenases to catalyze a variety of oxidative transformations on substrates ranging from small molecules to DNA via variations on the mechanism noted above imparted by different enzyme scaffolds. The

Related Fe(II)- and α KG-dependent halogenases (FeDHs) possess Fe(II) binding sites similar to those of FeDOs except that the conserved (Asp/Glu) residue in the Fe(II)-binding facial triad is replaced by Ala/Gly, providing space for a halide ligand ($X^- = Cl^-$, Br^-). The precise substrate positioning in the FeDH active site then leads to the chemoselective rebound of X^{\bullet} rather than HO $^{\bullet}$ to enable the site-selective chlorination or bromination of unactivated sp 3 C–H bonds under mild

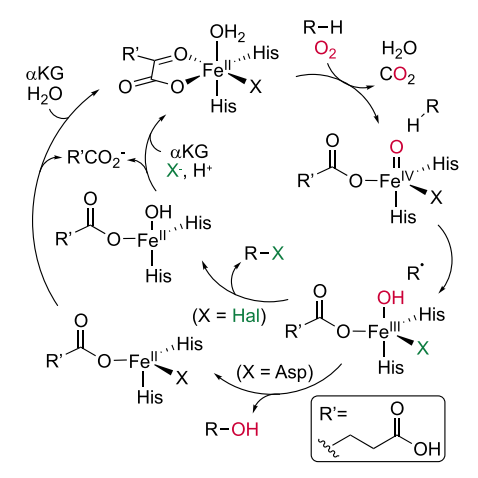


Figure 1. Simplified mechanisms for FeDO (outer cycle) and FeDH (inner cycle) catalysis.

Received: August 10, 2022 Published: August 31, 2022





conditions (Figure 1, inner cycle). The syrB2 was found to catalyze low levels of sp 3 C-H azidation and nitration (in addition to hydroxylation) in the presence of $X^- = N_3^-$ and NO_2^- (via N_3^{\bullet} and NO_2^{\bullet} rebound), and UV-vis spectroscopy was used to characterize the binding of an even broader range of anionic ligands to Fe(II) in this enzyme ($X^- = CN^-$, NCO^- , SH $^-$, and HCO_2^-). Subsequent studies have shown that other FeDHs can also catalyze azidation, but the relative levels of azidation and hydroxylation were not discussed. $^{11-13}$

Given the similar mechanisms of FeDOs and FeDHs, several studies have probed the origins of chemoselectivity for halogenation over oxygenation in the latter. 14-16 In addition to studying the substrate positioning in FeDHs, 7-9,17 researchers have investigated the effects of mutations to the conserved facial triad Asp/Glu residue in different FeDOs on the oxygenase activity of these enzymes, as extensively documented in a report of such efforts on TauD.¹⁸ A more limited number of studies described efforts to convert FeDOs to FeDHs by mutating the conserved facial triad Asp/Glu residue in different FeDOs to Ala/Gly. 18-20 These initial efforts typically resulted in significant decreases in hydroxylase activity, and while hydroxylase activity could be rescued to some extent in some of these efforts by the addition of specific anions, including halides, acetate, or formate, no halogenase activity was reported. More recently, similar facial triad variants of the FeDOs SadA (D157G)²¹ and SmP4H (D108G)²² revealed that modest levels of halogenase activity could be imparted to an FeDO in the presence of added chloride, though both of these cases still give primarily hydroxylation. These results show that a complete facial triad is required to support oxygenase chemistry¹⁹ and that exogenous anions can play a significant role in modulating the activity of a given FeDO containing a facial triad Asp/Glu-to-Gly mutation.

Beyond shedding light on the origins of FeDH chemoselectivity, understanding non-native anion effects on FeDO and FeDH activity is key to further developing non-native catalysis by these enzymes. As noted above, SadA D157G is one of only two examples in which a facial triad mutation results in halogenase activity,²¹ suggesting that it possesses relatively high promiscuity with respect to X* rebound. Moreover, the substrate tolerance of the native enzyme, which hydroxylated a variety of succinate-substituted amino acids, 23-25 also suggested that non-native activity could be extended to a broader range of substrates than has been reported to date. While only ~60% substrate conversion and ~30% selectivity for chlorination were reported for this enzyme (~18% conversion to chlorinated product),²¹ we reasoned that the apparent plasticity of the SadA active site with respect to both halide and organic substrate would make it a suitable system for studying anion effects on FeDO activity. Herein, we establish that a variety of anions can bind to an engineered variant of SadA D157G, hereafter SadX, that these anions accelerate hydroxylation catalysis by this enzyme, and that the enzyme catalyzes C-H functionalization using not only chloride and bromide but also azide and cyanate. Density functional theory (DFT) calculations were used to better understand both anion binding and rebound involving different iron intermediates relevant to catalysis. These results improve our understanding of the FeDO facial triad variant tolerance of different anionic ligands, their ability to promote rebound involving these ligands, and inherent rebound

preferences relative to HO[•] that will aid efforts to develop non-native catalysis using these enzymes.

METHODS

Materials. Unless otherwise noted, all reagents were obtained from commercial suppliers and used without further purification. A gene encoding SadA D157G was obtained as a synthetic gene from Integrated DNA Technologies (see the Supporting Information for sequence). Q5 HF DNA polymerase, Q5 reaction buffer, dNTPs, Dpn I, and Gibson Assembly Master Mix were purchased from New England Biolabs. Oligonucleotides were obtained from Integrated DNA Technologies. PrimeSTAR Max DNA Polymerase was purchased from Takara Bio USA. Ni-nitrilotriacetic acid (Ni-NTA) resin and Pierce BCA Protein Assay Kits were purchased from Fisher Scientific International, Inc., and the manufacturer's instructions were followed when using both products. Dowex 50WX8 strong cation exchange resin was purchased from Sigma-Aldrich.

SadX Activity Assays. Cloning, gene expression, and protein purification required to obtain SadX and related variants were conducted as described in the Supporting Information. SadX activity was analyzed in reactions prepared from three stock solutions. Solution A (1 mL containing 3 mM 1a, 30 µM enzyme, 0.3 mM $Fe(NH_4)_2(SO_4)_2$, and 24 mM ascorbic acid in 100 mM HEPES (pH 7.5)) was prepared by combining 300 μ L of 10 mM 1a, 300 μ L of 80 mM ascorbic acid, and 4.5 μ L of 2 mM enzyme, all in 100 mM HEPES (pH 7.5), with 365.5 μ L of 100 mM HEPES (pH 7.5) and 30 μ L of 10 mM Fe(NH₄)₂(SO₄)₂ in LC/MS-grade water (and stored on ice to avoid rapid air oxidation in the absence of ascorbic acid). Solutions B and C, containing 150 mM of the desired salt and 30 mM α KG, respectively, were prepared in 100 mM HEPES (pH 7.5). 30 μ L of solutions A-C was added to a 96-well v-bottom plate. The final reaction volume was 90 µL, and the reactions contained 1 mM substrate, 10 µM SadX (or variant), 50 mM salt (or no salt as a control), 0.1 mM Fe(NH₄)₂(SO₄)₂, 8 mM ascorbic acid, and 10 mM lphaKG. Plates were sealed with a breathable film and shaken at 750 rpm at room temperature overnight. The reactions were quenched the following day by the addition of methanol (90 μ L). The precipitated protein was then removed by centrifugation. The supernatant (60 μ L) was diluted with water (100 μ L), filtered, and analyzed by LC/MS with an injection volume of 0.5 μ L. Products and substrate peak areas in the resulting extract ion chromatograms were integrated on the Agilent MassHunter software. Product conversions were calculated using the relative peak area ratios between the product(s) and the substrate. Steady-state kinetic analysis was conducted in a similar fashion as described in the Supporting Information.

UV-Vis Titrations. A frozen solution of SadX-His (see the Supporting Information) was brought into a N2 glovebox using multiple cycles of evacuating and N2 flushing in the glovebox antechamber. Buffer was degassed in a Schlenk bomb by bubbling with N2 for 0.5 h and brought into the glovebox. Reagent solutions were prepared in the glovebox using the degassed buffer. A solution of SadX-His (0.51 mM, 985 μ L, 0.5 μ mol) and FeSO₄ (75 mM, 5 μ L, 0.375 µmol) in 100 mM HEPES (pH 7.50) at 23 °C was prepared in a quartz UV cuvette with a Schlenk adapter. The sample was carefully but thoroughly mixed with a glass pipette to avoid bubble formation and removed from the glovebox. The UV-vis spectra of the sample were recorded from 350 to 800 nm on a UV-vis spectrophotometer. The cuvette was returned to the glovebox, and a solution of αKG (500 mM, 10 μ L, 5 μ mol) in 100 mM HEPES (pH 7.5) was added. The sample had a volume of 1000 μ L; contained the final concentrations of 0.5 mM SadX-His, 0.375 mM Fe(II), and 2.5 mM α KG; and changed from pale yellow to pale pink upon the addition of α KG. The solution was carefully mixed, removed from the box, analyzed spectrophotometrically, and returned to the glovebox. A solution of the salt of interest (10, 25, 100, or 200 mM, 10 μ L) in 100 mM HEPES (pH 7.5) was added to the sample with a 25 μ L gas-tight syringe. The sample was gently tapped to mix, removed from the box, and analyzed spectrophotometrically. The titration was continued until saturation behavior was observed at the new metal-to-ligand

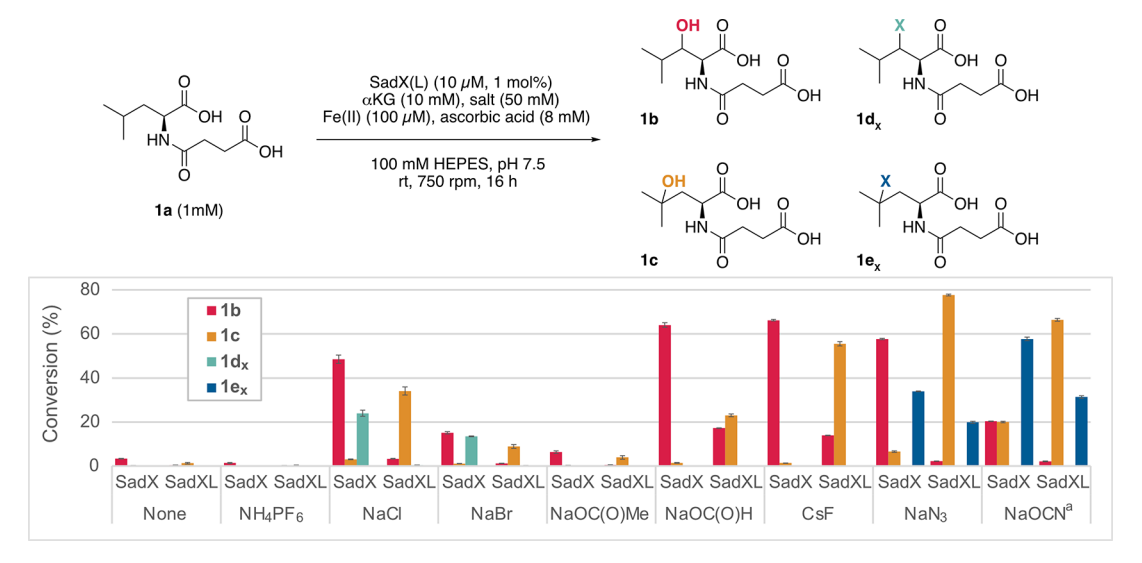


Figure 2. Reaction of 1a to produce products 1b/c and $1d_x/e_x$. Product conversions were calculated using the relative extracted ion chromatogram peak areas of products and the substrate obtained via LC/MS. Each data point represents the average of three replicates; the error bars represent standard deviations but are not visible for sufficiently small deviations. ^aConversion to a mixture of $1e_{OCN}$ and $1e_{NCO}$ as shown in Figure S15.

charge transfer (MLCT) band (~5–10 mM salt). Spectra were dilution-corrected, and difference spectra were obtained by subtracting the spectrum of the initial SadX-His/Fe(II) solution. Each difference spectrum was baseline-normalized by setting the absorbance difference at 800 nm to zero. Putative MLCT peaks were visualized by plotting the difference curves as a function of wavelength for each anion concentration. A single-site binding saturation model was used to fit the absorbances at different $\lambda_{\rm max}$ values, and $K_{\rm D}$ values were estimated using the software Prism 9.

Computational Methods. The primary coordination sphere of the Fe(II) center in SadX was modeled using the corresponding structure in the crystal structure of the FeDH WelO5¹⁻³ (PDB ID: SIQS). The model consisted of the Fe(II) metal center, a bidentate α ketoglutarate (α KG) ligand, two His ligands, a water ligand, and a chloride ligand (Figure S1). The His ligands were truncated at $C\beta$ (Figure S1). Hydrogen atoms were added to this model using Avogadro v1.2.0, and the N δ atoms of the His ligands and the distal carboxylate oxygen of α KG were protonated to produce a net neutral charge for the model (Figure S1). The universal force field (UFF)⁵ was used to relax all the added hydrogen atoms, while the heavy atoms were held fixed in Avogadro. Structures with other equatorial ligands were generated by replacing chloride with fluoride, hydroxide, water, azide, or formate (Figure S2). In the resulting structures, all heavy atoms except those of the new equatorial ligand were held fixed, and the ligand was relaxed with the UFF in Avogadro. All structures are neutral except for the one with water as an equatorial ligand, which has a +1 net charge.

Prior to computing the UV-vis spectra for the models of the aquo complexes with different anions, geometries were optimized by constraining the methyl carbon atoms of the truncated His ligands to mimic the His positions in the crystal structure (Figure S2). Optimizations were performed in ORCA⁶ v4.0.1.2 with DFT using the generalized gradient approximation (GGA) global hybrid PBE0 (with 25% exchange) and the def2-TZVP basis set.8 The semiempirical D39 dispersion correction was also included using the Becke-Johnson¹⁰ damping. All optimizations were carried out in high-spin (HS) quintet ground states, which were simulated with unrestricted calculations. All optimizations were carried out in redundant internal coordinates using the BFGS algorithm with default thresholds of 5 \times 10⁻⁶ hartree for the change in the selfconsistent field (SCF) energy between steps and 3 \times 10⁻⁴ hartree/ bohr for the maximum gradient. The conductor-like polarizable continuum model¹¹ (C-PCM) was used during geometry optimization in combination with the conductor-like screening solvent model (COSMO) epsilon function type obtained at the PBE0/def2-TZVP

level of theory with a solvent dielectric value, $\varepsilon=10$, approximately mimicking the protein environment. All calculations employed the resolution of identity (RI) approximation, $^{12-16}$ while the auxiliary basis set for def2-TZVP was generated automatically 17 by ORCA to accelerate calculations. Linear response time-dependent density functional theory (TD-DFT) calculations at the PBE0/def2-TZVP level of theory were used to simulate the UV–vis spectra of the optimized Fe(II)– α KG models within the Tamm–Dancoff approximation, 18 with the 30 lowest roots being converged. The C-PCM solvation model with a solvent dielectric value, $\varepsilon=10$, was used for both the ground and excited states (i.e., the linear response C-PCM model) to mimic the protein environment.

Models of the corresponding Fe(IV)-oxo and Fe(III)-hydroxo complexes with either a chloride or a fluoride ligand and a bidentate succinate ligand with the distal carboxylate oxygen protonated were generated with molSimplify, 19 which uses Open Babel 20,21 as a backend (Figure S3). These isomers possess an axial oxo/hydroxo ligand with an equatorial halide ligand or an equatorial oxo/hydroxo ligand with an axial halide ligand (Figure S3). Initial geometries for isomerization reaction coordinates (RCs) were generated using an inhouse Python script from optimized geometries of Fe(IV)-oxo isomers with monodentate succinate ²² (Figure S4). The isomerization RCs were sampled following the procedure in prior work²² by rotating oxo and/or halide ligands with respect to the axial His ligand in 1° increments of the angle formed by oxo/halide, Fe, and nitrogen of the axial His, from 90 to 180° (Figure S4). Constrained geometry optimizations along the isomerization RCs were carried out using ORCA v4.0.1.2 in the gas phase at the PBE0/def2-TZVP level of theory. For all optimizations, the methyl carbon atoms of the His ligands and all heavy atoms of succinate except the carboxylate bound to Fe were held fixed (Figure S4) to prevent rearrangements of the structure in a manner that would not be possible in the protein environment.

The radical rebound intermediates of the substrate and the Fe(III)-hydroxo complex were generated by modeling the substrate, *N*-succinyl-L-leucine, as 2-methylbutane to reduce the computational cost (Figure S5). RCs were obtained for the radical rebound reaction with both hydroxo and halide ligands by carrying out constrained optimizations in the gas phase using ORCA v4.0.1.2 at the B3LYP-D3/6-31G* level of theory. A smaller basis set was chosen for optimizations to reduce the computational cost. Heavy atom constraints applied during isomerization RCs were also applied (Figure S5). The constrained distance between radical carbon and oxygen of OH (·C···O) was varied in steps of 0.1 Å from 1.43 to 3.13 Å in RCs of the radical rebound of the hydroxo ligand on models of

both the chloro and fluoro complexes. Likewise, in RCs for the radical rebound of the halogen ligands (X), the distance between the radical carbon and the halogen ligand (\cdot C····X, X = Cl, F) was varied in steps of 0.1 Å from 1.82 to 3.52 Å for chloride and from 1.41 to 3.11 Å for fluoride.

High-energy structures along both isomerization RCs and radical rebound RCs were used to obtain vibrational frequencies. Gas-phase numerical Hessian calculations were carried out at the relevant level of theory, i.e., PBE0/def2-TZVP for isomerization RCs and B3LYP-D3/6-31G* for radical rebound RCs. The Hessian was computed using the central difference approach after 6N atomic displacements. The presence of an imaginary frequency along the RC confirmed that the high-energy structures along the RCs can be characterized as transition states. All initial and optimized structures for gas-phase and implicit solvent optimizations are provided in the Supporting Information.

RESULTS

Evaluation of SadX Activity. We first established that the expression of SadA D157G could be improved from 30-60 to 200-300 mg/L by fusing the enzyme to maltose-binding protein (MBP) to generate MBP-SadA D157G (SadX; Figure S13). We next assayed the activity of SadX on N-succinyl-Lleucine (1a), the substrate on which SadA D157G halogenase activity was demonstrated,²¹ in the presence of salts containing different anions, X- (Figure 2). Conversion to products resulting from C-H abstraction at different sites in 1a followed by the rebound of either HO^{\bullet} (1b/c) or X^{\bullet} (1d_x/e_x) was measured using extracted ion chromatograms obtained via LC/ MS. The salts had no effect on the activity of WT SadA,² which provided >99% conversion of la to lb in all cases (Figure S14). Salts containing a coordinating anion were essential for SadX activity, however, as only trace conversion was observed in their absence or in the presence of NH₄PF₆, which contained a non-coordinating PF₆⁻ anion. The latter result indicated that the increased ionic strength of the salt solutions was not responsible for the observed activity.

Rescue of SadX oxygenase activity was observed for all coordinating anions examined. Consistent with the previous report on SadA D157G activity,²¹ good conversion to 1b was observed in the presence of chloride, but bromide afforded significantly lower conversion. Acetate and formate were examined since they mimicked the native Asp residue of WT SadA. 18 While low conversion was observed using acetate, formate provided high conversion to 1b, suggesting that its smaller size was better accommodated by the D157G mutation. Azide, cyanate, and fluoride also provided high conversion to 1b, and a second hydroxylated product, 1c, also formed in the reactions containing azide and cyanate. In all cases, a single diastereomer of 1b was formed from enantiopure 1a, indicating that the stereoselectivity observed for WT SadA²³ was maintained in SadX variants in the presence of different anions.

In addition to rescuing oxygenase activity, four of the anions examined also led to the formation of two additional rebound products, $1d_x/e_x$. Low levels of chlorination and bromination resulted in single diastereomers of products $1d_{Cl}$ and $1d_{Br}$ as expected based on the previous report of this activity. Notably, however, both azide and cyanate also underwent reaction, in the former case leading to azidated product $1e_{N3}$ and in the latter leading to a mixture of two isomeric products, $1e_{OCN/NCO}$ (Figure S15). The isolation and characterization of $1e_{N3}$ revealed that its azide group was installed on C-4 of the substrate, as opposed to C-3 in the case of hydroxylation

(Figure S16). A similar site selectivity was also observed for (iso)cyanate insertion, and analysis of the product mixture by LC/MS indicated that the cyanate group was hydrated to give carbamates resulting from the rebound of both NCO $^{\bullet}$ and OCN $^{\bullet}$ such that $X = OC(O)NH_2$ and NHCO $_2H$ in $1e_{OCN/NCO}$. Specifically, the peak associated with the former co-eluted with a peak consistent with 1b/c in the total ion chromatogram, while the latter co-eluted with a peak consistent with the corresponding amine (Figure S15).

During ongoing efforts to alter the activity and selectivity of SadX, we found that SadX F152L (SadXL) provided C-4 hydroxylated product 1c (Figure S17) in the presence of all anions examined. SadXL selectivity for 1c over 1b was high for all anions except formate, and the enzyme also provided an improved selectivity for 1c over $1e_x$ relative to SadX selectivity for 1b over $1e_x$. Notably, reverting the facial triad mutation in SadXL (G157D) gave quantitative conversion to a 40:60 mixture of 1b and 1c, indicating that the high selectivity of SadXL for 1c in the presence of different anions resulted from the unique Fe(II) center created in the presence of these anions rather than by the enzyme scaffold alone.

Steady-State Kinetic Analysis of SadX Catalysis. To analyze the effects of representative anions more carefully on SadX activity, steady-state kinetic analysis of this enzyme was conducted using varying concentrations of substrate 1a (Figure 3 and Table 1). The catalytic efficiency $(k_{\rm cat}/K_{\rm M})$ of SadA in

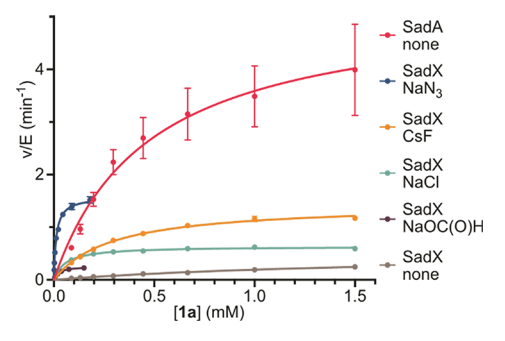


Figure 3. Initial rates of 1b formation in the presence of WT SadA or SadX and added salts as a function of [1a]. Each data point represents the average of three replicates; the error bars represent standard deviations but are not visible for sufficiently small deviations. Yields were determined by HPLC analysis relative to the *N*-acetyl-L-valine internal standard. The concentrations of 1a, salt, and enzyme are provided in Table 1.

our hands is similar to that previously reported, 23 but the $k_{\rm cat}/K_{\rm M}$ value for SadX in the absence of added salts is over 36-fold lower. This reduction results from both a reduced $k_{\rm cat}$ and an increased $K_{\rm M}$, again showing the importance of a complete facial triad to enable oxygenase catalysis. 19 Remarkably, the $k_{\rm cat}/K_{\rm M}$ for hydroxylation in the presence of added NaCl is nearly identical to that of WT SadA, and this rescue is achieved despite an eightfold reduction in $k_{\rm cat}$ because of a commensurate decrease in $K_{\rm M}$. An even greater decrease in $K_{\rm M}$ leads to a slightly higher $k_{\rm cat}/K_{\rm M}$ in the presence of NaOC(0)H. Even CsF gives a $k_{\rm cat}/K_{\rm M}$ value that is 16-fold improved relative to that observed in the absence of salt and only twofold lower than WT SadA. Finally, hydroxylation is significantly accelerated in the presence of NaN3, with $k_{\rm cat}/K_{\rm M}$ exceeding WT SadA by 12-fold, due to a decrease in $K_{\rm M}$.

The formation of azidated product $1e_{N3}$ also follows Michaelis-Menten kinetics (Figure S18 and Table 2). The

Table 1. Steady-State Kinetic Parameters for Hydroxylation of 1a to Give 1b in the Presence of Varying Concentrations of $1a^b$

enzyme (μM)	salt (mM)	[1a] (µM)	$(10^{-3} {\rm s}^{-1})$	$\binom{K_{ m M}}{({ m mM})}$	${k_{\rm cat}/K_{\rm M} \over { m (M^{-1}~s^{-1})}}$
SadA (0.1)	n/a	88-1500	88.1	0.473	186.3
SadX (0.5)	n/a	88-1500	8.77	1.715	5.1
SadX (0.5)	NaCl (50)	88-1500	10.6	0.058 ^a	182.8
SadX (0.1)	NaOC(0)H (50)	4.7-150	4.32	0.022	196.4
SadX (0.5)	CsF (50)	88-1500	24.1	0.286	84.3
SadX (0.1)	$NaN_3 (0.5)$	1.4-180	26.4	0.012	2200.0

 $[^]a The$ value represents an approximate K_M due to the lack of data acquired below 0.1 mM 1a. $^b n/a:$ not available.

Table 2. Steady-State Kinetic Parameters for Azidation and Chlorination of 1 by SadX to Give $1e_{\rm N3}$ and $1d_{\rm Cl}^{}$

salt	$k_{\rm cat} \ (10^{-3} \ {\rm s}^{-1})$	$K_{\rm M}~({ m mM})$	$k_{\rm cat}/K_{\rm M}~({ m M}^{-1}~{ m s}^{-1})$
NaN_3	8.72	0.011	792.7
NaCl		0.059	

^aThe concentrations of enzyme, salt, and 1a are provided in Table 1.

 $K_{\rm M}$ value for this reaction is comparable to that for the formation of ${\bf 1b}$ in the same reaction, but the $k_{\rm cat}$ value is one-third that for ${\bf 1b}$. The low $K_{\rm M}$ value nonetheless leads to a $k_{\rm cat}/K_{\rm M}$ value for the formation of ${\bf 1e}_{\rm N3}$ that is fourfold that for the formation of ${\bf 1b}$ by WT SadA. Finally, while a response factor was not measured for chlorinated product ${\bf 1d}_{\rm Cl}$, its formation in the presence of added chloride followed Michaelis—Menten kinetics, and a $K_{\rm M}$ value comparable to that for the formation of ${\bf 1b}$ in the same reaction was observed (Table 2).

Steady-state kinetic analysis of reactions conducted using a saturating concentration of ${\bf 1a}$ (1 mM) and different salt concentrations revealed that all coordinating anions examined (Cl⁻, F⁻, HCO₂⁻, and N₃⁻) exhibited saturation kinetics (Figure 4). The formation of ${\bf 1b}$ in the presence of NH₄PF₆ does not follow Michaelis—Menten kinetics, and varying its concentration has no effect on initial rates of the product formation. This kinetic behavior suggests that coordinating anions bind to Fe(II) and facilitate the production of ${\bf 1b}$ and

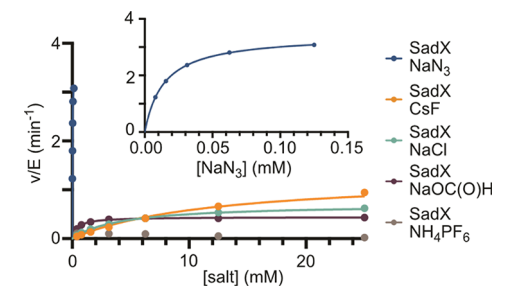


Figure 4. Initial rates of **1b** formation from 1 mM **1a** catalyzed by 0.5 μ M SadX as a function of [salt]. Each data point represents the average of three replicates; the error bars represent standard deviations but are not visible for sufficiently small deviations. Yields were determined by HPLC analysis relative to the *N*-acetyl-L-valine internal standard. The concentrations of salts are provided in Table 3.

 $1d_x/e_x$. Values for $k_{\rm cat}/K_{\rm M}$ in the presence of salts with coordinating anions follow the trend N₃⁻ > HCO₂⁻ > Cl⁻ > F⁻, largely as a result of the respective $K_{\rm M}$ values, which span three orders of magnitude (Table 3). These results again suggest that both the electronic properties and the size of different coordinating anions modulate their ability to rescue oxygenase catalysis (Table 2).

Table 3. Steady-State Kinetic Parameters for Hydroxylation of 1a by SadX to Give 1b in the Presence of Varying Concentrations of Salt^b

salt ^a	$k_{\rm cat}~({\rm min}^{-1})$	$K_{\rm M}~({\rm mM})$	$k_{\rm cat}/K_{\rm M}~({ m M}^{-1}~{ m s}^{-1})$
NH_4PF_6	n/a	n/a	n/a
NaCl	11.8	4.16	2.84
NaOC(O)H	7.35	0.45	16.33
CsF	21.4	11.98	1.79
NaN_3	57.2	0.014	4085

"[Salt] was varied from 0.39 to 50 mM except for [NaN $_3$], which was varied from 0.0078 to 1 mM. b n/a: not available.

Analysis of Anion Binding via UV-Vis Spectroscopy.

UV—vis spectroscopy was next used to measure anion binding to the Fe(II) center in SadX. Fe(II)- and α KG-dependent enzymes exhibit a characteristic Fe(II) $\rightarrow \alpha$ KG MLCT band near 500 nm. Previous analysis of the FeDH SyrB2 and a facial triad mutant (D201G) of the FeDO FIH showed that titrating samples of these enzymes with different anions led to anion-dependent shifts in the $\lambda_{\rm max}$ values of this diagnostic MLCT band corresponding to the formation of different anion-substituted Fe(II) centers. The difference spectra for the resulting titration data can then be used to construct binding isotherms to determine the $K_{\rm D}$ values for different anions. In general, peaks in the absorbance spectra for SadX broaden upon the addition of different anions (X = Cl⁻, F⁻, N₃⁻, and HCO₂⁻). This broadening results from apparent absorption bands at ~450 and ~600 nm (Figure 5A–D).

Computed UV-Vis Transitions for SadX Model **Complexes.** Because two absorptions appear in the difference spectra shown in Figure 5, the UV-vis spectra are calculated for models of the primary coordination sphere of the Fe(II) aguo intermediates in SadX with relevant anions bound (see Methods for details) to identify which of these absorptions corresponds to the MLCT. For example, the calculated UVvis spectrum for the chloride complex shows a strong peak at 617 nm. Examining the transition density, which represents the density difference between the ground and excited states, corresponding to the transition at 617 nm shows a change in density on both Fe and α KG, indicating either an MLCT or a ligand-to-metal charge transfer (LMCT) state (Figure 6). Analysis of natural transition orbitals²³ (NTOs) reveals the presence of higher density on Fe and lower density on α KG in the initial state and the reverse in the final state, confirming that the transition at 617 nm is an MLCT (Figure 6). While transitions at both blue- and red-shifted wavelengths are observed experimentally, the computational UV-vis spectrum suggests that the MLCT is observed at the red-shifted wavelength of 643 nm.

While good agreement between the computed MLCT and the observed UV-vis spectra was obtained for the chloro complex, a similar agreement was not obtained for complexes of the other anions investigated (Table 4 and Figures S19-S24). Notably, the computed Fe-Cl bond length in the

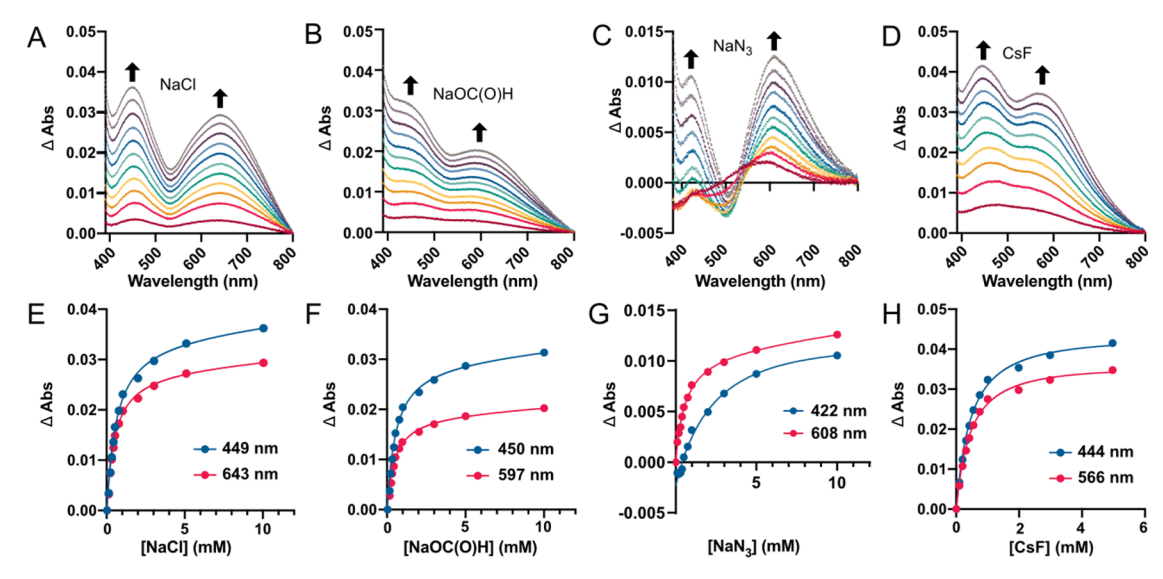


Figure 5. (A–D) Difference UV–vis spectra of samples of SadX with increasing concentrations of different salts. (E–H) Binding isotherms for anion binding to the Fe(II) center in SadX constructed from the UV–vis difference spectra.

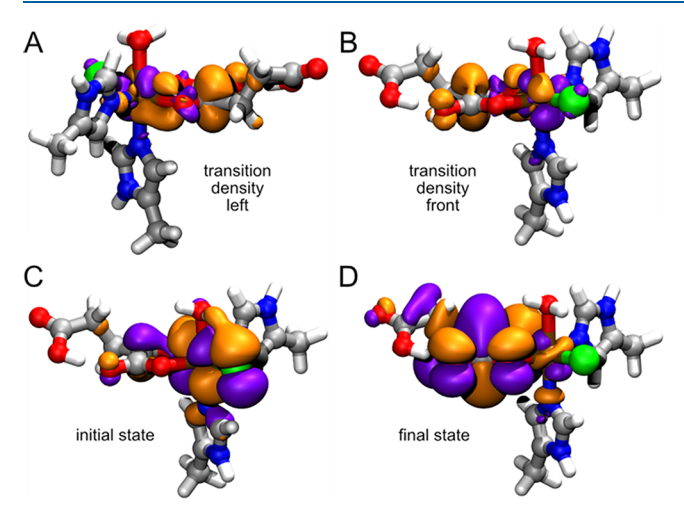


Figure 6. (A) Left and (B) front views of transition densities and natural transition orbitals (NTOs) of (C) initial and (D) final states corresponding to an MLCT transition at 617 nm in the computational UV—vis spectra of the optimized $Fe(II)/\alpha KG$ aquo complex with a chloride ligand. Atoms are colored as H in white, C in silver, N in blue, O in red, Cl in green, and Fe in brown. Purple indicates the positive wave function phase, and orange indicates the negative wave function phase in the isosurfaces. An isosurface value of 0.0009 $e^-/$ bohr³ is used for transition density visualization, while an isosurface value of 0.01 $e^-/$ bohr³ is used for NTO visualizations.

Table 4. $\lambda_{\rm max}$ and $K_{\rm D}$ Values Obtained from Anion Titration Experiments and MLCT Transitions from the Computed UV–Vis Spectra

	blue-shifted absorbance			hifted bance	computed MLCT
X ligand	$\begin{pmatrix} \lambda_{\max} \\ (nm) \end{pmatrix}$	$\frac{K_{\mathrm{D}}}{(\mathrm{mM})}$	λ_{\max} (nm)	$\frac{K_{\mathrm{D}}}{(\mathrm{mM})}$	λ (nm)
NaCl	449	0.60	643	0.49	617
CsF	444	0.46	566	0.45	335
NaN_3	422	2.65	608	0.60	360, 390
NaOC(O)H	450	0.53	597	0.47	354, 398

optimized geometry of the chloro complex is 2.43 Å, which is comparable to Fe-Cl bond lengths observed in the crystal structures of FeDHs SyrB2²⁴ (PDB ID: 2FCT) and BesD²⁵ (PDB ID: 6NIE; Table S3). The computed UV-vis spectrum of a representative model of the active site of SyrB2 indicates an MLCT from Fe to α KG at a red-shifted wavelength of 758 nm, which is consistent with the red-shifted wavelength for MLCT observed with the optimized geometry of the active site of WelO5 (Figure S25). On the other hand, the Fe-Cl bond length in the crystal structure of the FeDH WelO5¹ (PDB ID: SIQS) is relatively short in comparison (Table S3). This bond length increases upon the gas-phase geometry optimization of the extracted Fe(II) aquo complex, suggesting that the protein environment enforces a shorter Fe-Cl bond in WelO5. The computed UV-vis spectrum of the Fe(II) aquo complex from WelO5 shows an MLCT that is blue-shifted relative to the same complex following geometry optimization (Figure S19 and Figure 1).

To understand the effect of the Fe-Cl bond length on the observed MLCT wavelengths for the SadX Fe(II) aquo model complex, the UV-vis spectra for this complex were calculated at different Fe-Cl bond lengths. At shorter Fe-Cl bond lengths, i.e., between 1.8 and 2.2 Å (i.e., shorter than the equilibrium bond length by ca. 0.2-0.6 Å), the MLCT is blueshifted (Table S4), but as the Fe-Cl bond length increases (2.2-2.5 Å), the MLCT is red-shifted (Table S4). This finding indicates that the assigned MLCT wavelength is dependent on the Fe-Cl bond length. A similar variation for other anions would lead to analogous differences between the computed and experimental spectra that would depend on the orientation of the anion within SadX. Understanding the origin(s) of these differences in a more complete active site model could shed light on the nature of anion binding within SadX. Coincidently, however, similar binding affinities ($K_D = 0.45-0.60 \text{ mM}$) were obtained from analysis of binding isotherms constructed from the difference spectra at either the blue- or red-shifted wavelengths for all but the blue-shifted absorbance for azide $(K_D = 6.0 \text{ mM})$, so precisely defining the MLCT was not required to establish anion binding affinities.

Computational Analysis of Anion Effects on C-OH/X Rebound Barriers. The steady-state kinetic characterization

of SadX indicates that a variety of anions significantly accelerate SadX C–H hydroxylation catalysis. Formate and fluoride are unique in that they are strongly activating ligands that do not undergo significant rebound. The latter result is notable since both chloride and bromide ligands undergo rebound to form C–Cl and C–Br bonds, respectively. Focusing on the halide series, these results suggest that Fe(III)(OH)(X) intermediates involved in the HO^{\bullet}/X^{\bullet} rebound step of FeDO/H catalysis (Figure 1) can form with X = F, Cl, and Br. To better understand why X rebound is observed for X = Cl and Br but not for X = F, we conducted a computational analysis of the barriers associated with HO^{\bullet} and X^{\bullet} rebound from Fe(III)(OH)(X), where X = Cl and F.

Previous computational analysis has shown that radical rebound in FeDHs can involve either axial or equatorial X/OH ligands of Fe(III)(OH)(X) intermediates. In these studies, energies for axial and equatorial rebound are similar, so analysis of the axial pathway was studied in the current case (Supporting Text S1, Figures S6-S9, and Tables S1 and S2). The computed free energies of reaction for the rebound of HO*, Cl*, and F* are all highly exergonic (Figures S10 and S11); the HO^{\bullet} rebound is comparable for both X = Cl and F(ca. -58 kcal/mol) and much more favorable than the rebound of either Cl^o or F^o (ca. -35 and -30 kcal/mol, respectively). The barriers for each of these processes were next calculated. The computed free energy of activation for the HO rebound was near zero for X = Cl with a C···O-H distance of 1.43 Å, but a barrier of ~3 kcal/mol and a C···O-H distance of 2.43 Å were observed for X = F (Figure S10). We also obtained the HO rebound reaction coordinate by adding Arg residues in the active site and modeling succinate as monodentate. We observe that for X = F, the reaction is barrierless (a minor barrier of ca. 1 kcal/mol) compared to ~3 kcal/mol observed without Arg residues (Figure S10). We observe a similar barrierless rebound reaction coordinate for X = Cl (Figure S10). The rebound of Cl* and F* proceeded with barriers of 1.4 kcal/mol (C···Cl distance: 2.62 Å) and 6.5 kcal/ mol (C···F distance: 2.11 Å), respectively (Figure S11). We further optimized the transition state along the Cl^o rebound reaction coordinate, where the C···Cl distance is 2.65 Å, which is comparable to the corresponding C···Cl distance of 2.62 Å in the highest energy structure observed from the relaxed scan along the reaction coordinate. The imaginary frequency corresponding to the C···Cl stretch in the optimized transition state is 137 cm⁻¹, which is comparable to 156 cm⁻¹ observed for the highest energy structure along the reaction coordinate.

DISCUSSION

An increasing body of research on non-native enzyme catalysis has established that enzymes can catalyze chemical reactions distinct from, yet mechanistically related to, those for which they naturally evolved. The potential to harness this capability for non-directed C-H functionalization is appealing since controlling the site selectivity of such reactions remains a significant synthetic challenge. FeDHs and FeDO facial triad variants are notable in this regard since they offer the potential to decouple the C-H activation and C-X bond formation steps of C-H functionalization processes. C-H activation by these enzymes proceeds via an Fe(IV)-oxo intermediate bearing an additional anionic ligand, X-. If the rebound of X can be favored over HO from the resulting Fe(III)(OH)(X) intermediate, then, in principle, any number of anionic ligands could be used for C-H functionalization.

Harnessing this potential reactivity, however, requires both a basic understanding of which anionic ligands can undergo rebound and their inherent rebound preferences relative to HO^{\bullet} .

In this study, we explored the binding of different anions to SadA D157G fused to MBP, which we have termed SadX, and the effects of that binding on HO vs X rebound. Previous studies have established that SadA can hydroxylate various Nsuccinylated amino acids²³ and that SadA D157G catalyzes chlorination and bromination of N-succinyl-L-leucine, 21 albeit to a minor extent relative to hydroxylation. We established not only that chloride and bromide enabled these non-native halogenation reactions but also that all anions investigated significantly accelerated hydroxylation catalysis by SadX. While SadX activity in the absence of added salt is minimal, adding either NaCl or NaOC(O)H restores hydroxylase activity to that of WT SadA, and adding azide leads to hydroxylation rates 12-fold higher than those of the WT enzyme. Successful rescue of hydroxylase activity in FeDO facial triad variants using exogenous anions remains rare and typically leads to activities that are below those of the WT enzymes. 18,19 Our results show that the unique steric and electronic properties created by nonnative anion binding to the Fe(II) center of SadX lead to oxygenase activity that exceeds that capable with the native Asp residue and reaffirm the observation that a complete primary coordination sphere is required for FeDO/X catalysis. 19

Our findings also show that anion binding also influences FeDO site selectivity. For example, SadX favors the formation of 1b (>80:20 1b:1c) for all anions examined except cyanate, but SadXL favors the formation of 1c under the same conditions, showing how the SadX/L scaffold can control site selectivity. On the other hand, reverting the D157G mutation in SadXL to give SadA F152L leads to the formation of a 40:60 mixture of 1b:1c, indicating that the F152L mutation alone is insufficient to achieve the high selectivity of SadXL for the formation of 1c in the presence different anions. This effect is particularly notable for fluoride since this anion gives rise to the largest switch in site selectivity without affecting chemoselectivity; in the presence of CsF, SadX gives a 1b:1c ratio of nearly 50:1, while SadXL gives a 1b:1c ratio of 1:4.

In addition to altering hydroxylase activity and selectivity, NaN₃ and NaOCN lead to the formation of products resulting from an extent of N_3^{\bullet} , NCO $^{\bullet}$, and OCN $^{\bullet}$ rebound that is greater than the extent of Cl°/Br° rebound observed in the presence of NaCl/Br. While FeDHs such as SyrB2 and SaDAH also form azidated products in the presence of NaN₃, ^{10,12} SadX is the first example of an FeDO facial triad variant that catalyzes azidation and the first of either enzyme class to catalyze the incorporation of cyanate into a molecule. Here again, anions appear to alter selectivity, with both azide and cyanate preferring functionalization at the tertiary carbon of 1a to give $1e_{\rm N3}$ and $1e_{\rm OCN/NCO}$. SadX-catalyzed azidation is also more efficient than hydroxylation by WT SadA. Similar K_M values were measured for both azidation/hydroxylation and chlorination/hydroxylation of 1a, suggesting a similar binding of 1a within the SadX active site regardless of whether it undergoes azidation/chlorination or hydroxylation.

Previous studies have established that anions bind to both FeDHs and FeDOs with similar affinities, 10 and a similar behavior in $K_{\rm D}$ was observed for SadX, despite the very different $K_{\rm M}$ values observed for hydroxylation of 1a in the presence of different anions. The observed fluoride binding is

notable since it was not observed to a significant extent in SyrB2¹⁰ or FIH D201G.¹⁹ Fluoride-accelerated hydroxylation³² is even more notable since it suggests that fluoride is bound to the Fe(III)(OH)(F) intermediate during hydroxylation catalysis and begs the question as to why SadX does not catalyze the fluorination of 1a. DFT calculations suggest that the lack of fluorination is not necessarily due to a high barrier (ΔG^{\ddagger}) to F^{\bullet} rebound, which was calculated in this study to be only 6.5 kcal/mol and has been characterized using high-valent iron fluoride corrole model complexes³¹ and calculated to be 3.0 kcal/mol in a study on an Fe(III)(OH)(F) model complex.³³ Instead, the lack of fluorination in the current cases is more likely due to a 3.5 kcal/mol $\Delta\Delta G^{\ddagger}$ between the transition states associated with HO* and F* rebound from the Fe(III)(OH)(F) complex (Figure S12). The calculated $\Delta\Delta G^{\ddagger}$ for the corresponding chloride complex is only ~1.4 kcal/mol. These $\Delta \Delta G^{\ddagger}$ values correspond to inherent differences in rates of rebound for OH/X of $\sim 10 \times$ and $\sim 260 \times$ for X = Cl[•] and F[•], respectively, in which an enzyme would have to overcome to enable these reactions. These relative rates are qualitatively consistent with the experimental observation that chlorination is not observed, albeit as a minor product relative to hydroxylation, but that no significant fluorination is observed. Both values are low enough that one might expect the enzyme scaffold to provide access to improved levels of chlorination and perhaps even fluorination.

CONCLUSIONS

In this study,³⁴ we explored the binding of different anions, X⁻, to an FeDO facial triad variant, SadX, and the effects of anion binding on HO and X rebound. Spectrophotometric titrations revealed that several anions known to bind the Fe(II) center of other FeDHs and FeDO facial triad variants also bound to SadX, and evidence for fluoride binding not reported for other systems was also observed. All anions that bound the Fe(II) center of SadX also accelerated hydroxylation catalysis by this enzyme, which also catalyzed C-H functionalization using not only chloride and bromide but also azide and cyanate. DFT calculations were used to better understand both anion binding and rebound involving different Fe intermediates relevant to SadX catalysis. These calculations suggest that the lack of fluorination is due to the relative barriers of the HO and F rebound transition states rather than an inaccessible barrier for F° rebound. Together, these results improve our understanding of the FeDO facial triad variant tolerance of different anionic ligands, their ability to promote rebound involving these ligands, and inherent rebound preferences relative to HO° that will aid efforts to develop non-native catalysis using these enzymes.

ASSOCIATED CONTENT

Supporting Information

The Supporting Information is available free of charge at https://pubs.acs.org/doi/10.1021/acs.inorgchem.2c02872.

Supplementary figures, complete experimental procedures, computational details, and relevant characterization (PDF)

All assay data described in this manuscript (XLSX)

AUTHOR INFORMATION

Corresponding Authors

Heather J. Kulik – Department of Chemical Engineering, Massachusetts Institute of Technology, Cambridge, Massachusetts 02139, United States; oorcid.org/0000-0001-9342-0191; Email: hjkulik@mit.edu

Jared C. Lewis — Department of Chemistry, Indiana University, Bloomington, Indiana 47405, United States; orcid.org/0000-0003-2800-8330; Email: jcl3@iu.edu

Authors

Natalie H. Chan — Department of Chemistry, Indiana University, Bloomington, Indiana 47405, United States Christian A. Gomez — Department of Chemistry, Indiana University, Bloomington, Indiana 47405, United States Vyshnavi Vennelakanti — Department of Chemical Engineering, Massachusetts Institute of Technology.

Engineering, Massachusetts Institute of Technology, Cambridge, Massachusetts 02139, United States;
orcid.org/0000-0001-7677-2902

Qian Du – Department of Chemistry, Indiana University, Bloomington, Indiana 47405, United States

Complete contact information is available at: https://pubs.acs.org/10.1021/acs.inorgchem.2c02872

Author Contributions

§These authors contributed equally to this study.

Notes

The authors declare no competing financial interest.

ACKNOWLEDGMENTS

This study was supported by the NIH (R01 GM115665 to J.C.L.) and by the NSF under the CCI Center for Selective C—H Functionalization (CCHF, CHE-1205646 to J.C.L.). H.J.K. and V.V. were supported by the NSF under grant numbers CBET-1846426 and CBET-1704266. H.J.K. holds a Career Award at the Scientific Interface from the Burroughs Wellcome Fund, which supported this work. We thank Dr. Dibyendu Mondal for his assistance in the synthesis of the substrate *N*-succinyl-L-leucine.

■ REFERENCES

- (1) Hausinger, R. P. Fe(II)/ α -Ketoglutarate-Dependent Hydroxylases and Related Enzymes. *Crit. Rev. Biochem. Mol. Biol.* **2004**, 39, 21–68.
- (2) Martinez, S.; Hausinger, R. P. Catalytic Mechanisms of Fe(II)-and 2-Oxoglutarate-Dependent Oxygenases. *J. Biol. Chem.* **2015**, 290, 20702–20711.
- (3) Straganz, G. D.; Nidetzky, B. Variations of the 2-His-1-Carboxylate Theme in Mononuclear Non-Heme FeII Oxygenases. 2006, 7 (10), 1536–1548, DOI: 10.1002/cbic.200600152.
- (4) Papadopoulou, A.; Meyer, F.; Buller, R. M. Engineering Fe(II)/ α -Ketoglutarate-Dependent Halogenases and Desaturases. *Biochemistry* **2022**, DOI: 10.1021/acs.biochem.2c00115.
- (5) Timmins, A.; de Visser, S. P. A Comparative Review on the Catalytic Mechanism of Nonheme Iron Hydroxylases and Halogenases. *Catalysts* **2018**, *8*, 314–325.
- (6) Voss, M.; Malca, S. H.; Buller, R. Exploring the Biocatalytic Potential of Fe/A-Ketoglutarate-Dependent Halogenases. *Chem. Eur. J.* **2020**, *26*, 7336–7345.
- (7) Mehmood, R.; Qi, H. W.; Steeves, A. H.; Kulik, H. J. The Protein's Role in Substrate Positioning and Reactivity for Biosynthetic Enzyme Complexes: The Case of SyrB2/SyrB1. *ACS Catal.* **2019**, 4930.

- (8) Matthews, M. L.; Neumann, C. S.; Miles, L. A.; Grove, T. L.; Booker, S. J.; Krebs, C.; Walsh, C. T.; Bollinger, J. M., Jr. Substrate Positioning Controls the Partition between Halogenation and Hydroxylation in the Aliphatic Halogenase, SyrB2. *Proc. Natl. Acad. Sci.* **2009**, *106*, 17723–17728.
- (9) Martinie, R. J.; Livada, J.; Chang, W. C.; Green, M. T.; Krebs, C.; Bollinger, J. M., Jr.; Silakov, A. Experimental Correlation of Substrate Position with Reaction Outcome in the Aliphatic Halogenase, SyrB2. *J. Am. Chem. Soc.* **2015**, *137*, 6912–6919.
- (10) Matthews, M. L.; Chang, W.-C.; Layne, A. P.; Miles, L. A.; Krebs, C.; Bollinger, J. M., Jr. Direct Nitration and Azidation of Aliphatic Carbons by an Iron-Dependent Halogenase. *Nat. Chem. Biol.* **2014**, *10*, 209–215.
- (11) Büchler, J.; Malca, S. H.; Patsch, D.; Voss, M.; Turner, N. J.; Bornscheuer, U. T.; Allemann, O.; Le Chapelain, C.; Lumbroso, A.; Loiseleur, O.; Buller, R. Algorithm-Aided Engineering of Aliphatic Halogenase WelO5* for the Asymmetric Late-Stage Functionalization of Soraphens. *Nat. Commun.* 2022, *13*, 371.
- (12) Kim, C. Y.; Mitchell, A. J.; Glinkerman, C. M.; Li, F.-S.; Pluskal, T.; Weng, J.-K. The Chloroalkaloid (—)-Acutumine Is Biosynthesized via a Fe(II)- and 2-Oxoglutarate-Dependent Halogenase in Menispermaceae Plants. *Nat. Commun.* **2020**, *11*, 1867.
- (13) Neugebauer, M. E.; Sumida, K. H.; Pelton, J. G.; McMurry, J. L.; Marchand, J. A.; Chang, M. C. Y. A Family of Radical Halogenases for the Engineering of Amino-Acid-Based Products. *Nat. Chem. Biol.* **2019**, *15*, 1009–1016.
- (14) Wong, C.; Fujimori, D. G.; Walsh, C. T.; Drennan, C. L. Structural Analysis of an Open Active Site Conformation of Nonheme Iron Halogenase CytC3. J. Am. Chem. Soc. 2009, 131, 4872–4879.
- (15) Vaillancourt, F. H.; Yin, J.; Walsh, C. T. SyrB2 in Syringomycin E Biosynthesis Is a Nonherne Fe-II α -Ketoglutarate- and O-2-Dependent Halogenase. *Proc. Natl. Acad. Sci. U. S. A.* **2005**, *102*, 10111–10116.
- (16) Blasiak, L. C.; Vaillancourt, F. H.; Walsh, C. T.; Drennan, C. L. Crystal Structure of the Non-Haem Iron Halogenase SyrB2 in Syringomycin Biosynthesis. *Nature* **2006**, *440*, 368–371.
- (17) Pan, J.; Wenger, E. S.; Matthews, M. L.; Pollock, C. J.; Bhardwaj, M.; Kim, A. J.; Allen, B. D.; Grossman, R. B.; Krebs, C.; Bollinger, J. M., Jr. Evidence for Modulation of Oxygen Rebound Rate in Control of Outcome by Iron(II)- and 2-Oxoglutarate-Dependent Oxygenases. J. Am. Chem. Soc. 2019, 141, 15153—15165.
- (18) Grzyska, P. K.; Müller, T. A.; Campbell, M. G.; Hausinger, R. P. Metal Ligand Substitution and Evidence for Quinone Formation in Taurine/ α -Ketoglutarate Dioxygenase. *J. Inorg. Biochem.* **2007**, *101*, 797–808.
- (19) Chaplin, V. D.; Hangasky, J. A.; Huang, H.-T.; Duan, R.; Maroney, M. J.; Knapp, M. J. Chloride Supports O2 Activation in the D201G Facial Triad Variant of Factor-Inhibiting Hypoxia Inducible Factor, an α -Ketoglutarate Dependent Oxygenase. *Inorg. Chem.* **2018**, 57, 12588–12595.
- (20) Gorres, K. L.; Pua, K. H.; Raines, R. T. Stringency of the 2-His-1-Asp Active-Site Motif in Prolyl 4-Hydroxylase. *PLoS One* **2009**, *4*, No. e7635.
- (21) Mitchell, A. J.; Dunham, N. P.; Bergman, J. A.; Wang, B.; Zhu, Q.; Chang, W.; Liu, X.; Boal, A. K. Structure-Guided Reprogramming of a Hydroxylase To Halogenate Its Small Molecule Substrate. *Biochemistry* **2017**, *56*, 441–444.
- (22) Papadopoulou, A.; Meierhofer, J.; Meyer, F.; Hayashi, T.; Schneider, S.; Sager, E.; Buller, R. Re-Programming and Optimization of a L-Proline Cis-4-Hydroxylase for the Cis-3-Halogenation of Its Native Substrate. *ChemCatChem* **2021**, *13*, 3914–3919.
- (23) Hibi, M.; Kasahara, T.; Kawashima, T.; Yajima, H.; Kozono, S.; Smirnov, S. V.; Kodera, T.; Sugiyama, M.; Shimizu, S.; Yokozeki, K.; Ogawa, J. Multi-Enzymatic Synthesis of Optically Pure β -Hydroxy α -Amino Acids. *Adv. Synth. Catal.* **2015**, *357*, 767–774.
- (24) Qin, H.-M.; Miyakawa, T.; Nakamura, A.; Hibi, M.; Ogawa, J.; Tanokura, M. Structural Optimization of SadA, an Fe(II)- and α -Ketoglutarate-Dependent Dioxygenase Targeting Biocatalytic Syn-

- thesis of N-Succinyl-l-Threo-3,4-Dimethoxyphenylserine. *Biochem. Biophys. Res. Commun.* **2014**, 450, 1458–1461.
- (25) Qin, H.-M.; Miyakawa, T.; Jia, M. Z.; Nakamura, A.; Ohtsuka, J.; Xue, Y.-L.; Kawashima, T.; Kasahara, T.; Hibi, M.; Ogawa, J.; Tanokura, M. Crystal Structure of a Novel N-Substituted L-Amino Acid Dioxygenase from Burkholderia Ambifaria AMMD. *PLoS One* **2013**, *8*, e63996–e63999.
- (26) Solomon, E. I.; Brunold, T. C.; Davis, M. I.; Kemsley, J. N.; Lee, S.-K.; Lehnert, N.; Neese, F.; Skulan, A. J.; Yang, Y.-S.; Zhou, J. Geometric and Electronic Structure/Function Correlations in Non-Heme Iron Enzymes. *Chem. Rev.* **2000**, *100*, 235–350.
- (27) Prier, C. K.; Arnold, F. H. Chemomimetic Biocatalysis: Exploiting the Synthetic Potential of Cofactor-Dependent Enzymes To Create New Catalysts. *J. Am. Chem. Soc.* **2015**, *137*, 13992–14006.
- (28) Lewis, J. C.; Coelho, P. S.; Arnold, F. H. Enzymatic Functionalization of Carbon-Hydrogen Bonds. *Chem. Soc. Rev.* **2011**, *40*, 2003–2021.
- (29) Kuhl, N.; Hopkinson, M. N.; Wencel-Delord, J.; Glorius, F. Beyond Directing Groups: Transition-Metal-Catalyzed C-H Activation of Simple Arenes. *Angew. Chem., Int. Ed. Eng.* **2012**, *51*, 10236–10254.
- (30) Yadav, V.; Rodriguez, R. J.; Siegler, M. A.; Goldberg, D. P. Determining the Inherent Selectivity for Carbon Radical Hydroxylation versus Halogenation with FeIII(OH)(X) Complexes: Relevance to the Rebound Step in Non-Heme Iron Halogenases. *J. Am. Chem. Soc.* **2020**, *142*, 7259–7264.
- (31) Farley, G. W.; Siegler, M. A.; Goldberg, D. P. Halogen Transfer to Carbon Radicals by High-Valent Iron Chloride and Iron Fluoride Corroles. *Inorg. Chem.* **2021**, *60*, 17288–17302.
- (32) Tsygankov, A. A.; Chusov, D. Straightforward Access to High-Performance Organometallic Catalysts by Fluoride Activation: Proof of Principle on Asymmetric Cyanation, Asymmetric Michael Addition, CO2 Addition to Epoxide, and Reductive Alkylation of Amines by Tetrahydrofuran. ACS Catal. 2021, 11, 13077–13084.
- (33) Gérard, E. F.; Yadav, V.; Goldberg, D. P.; de Visser, S. P. What Drives Radical Halogenation versus Hydroxylation in Mononuclear Nonheme Iron Complexes? A Combined Experimental and Computational Study. *J. Am. Chem. Soc.* **2022**, *144*, 10752–10767.
- (34) Chan, N. H.; Gomez, C.; Vennelakanti, V.; Du, Q.; Kulik, H. J.; Lewis, J. C. Non-Native Anionic Ligand Binding and Reactivity in Engineered Variants of the Fe(II)- and α -Ketoglutarate-Dependent Oxygenase, SadA. *ChemRxiv* [*Preprint*], *May* 23, 2022 *Version* 2, DOI: 10.26434/chemrxiv-2022-8h07c-v2.